bioRxiv preprint doi: https://doi.org/10.1101/614172; this version posted April 23, 2019. The copyright holder for this preprint (which was not certified by peer review) is the author/funder, who has granted bioRxiv a license to display the preprint in perpetuity. It is made available under aCC-BY-NC-ND 4.0 International license.

Title:

All-optical electrophysiology reveals excitation, inhibition, and neuromodulation in cortical layer 1

Authors: Linlin Z. Fan[1], Simon Kheifets[1], Urs L. Böhm[1], Kiryl D. Piatkevich[2], Hao Wu[1], Vicente Parot[1], Michael E. Xie[1], Edward S. Boyden[2], Anne E. Takesian[3,4], Adam E. Cohen[1,5,6,*]

Affiliations:

[1]Department of Chemistry and Chemical Biology, Harvard University, Cambridge, MA, USA

[2]Media Lab and McGovern Institute for Brain Research, Massachusetts Institute of Technology (MIT), Cambridge, MA, USA

[3]Harvard Medical School, Boston, USA

[4]Massachusetts Eye and Ear Infirmary, Boston, USA

[5]Department of Physics, Harvard University, Cambridge, MA USA

[6]Howard Hughes Medical Institute

*Correspondence to: cohen@chemistry.harvard.edu

Abstract: The stability of neural dynamics arises through a tight coupling of excitatory (E) and inhibitory (I) signals. Genetically encoded voltage indicators (GEVIs) can report both spikes and subthreshold dynamics *in vivo*, but voltage alone only reveals the combined effects of E and I synaptic inputs, not their separate contributions individually. Here we combine optical recording of membrane voltage with simultaneous optogenetic manipulation to probe E and I individually in barrel cortex Layer 1 (L1) neurons in awake mice. Our studies show that L1 neurons integrate thalamocortical excitation and lateral inhibition to produce precisely timed responses to whisker stimuli. Top-down neuromodulatory inputs drive additional excitation in L1. Together, these results suggest a model for computation in L1 consistent with its hypothesized role in attentional gating of the underlying cortex.

One Sentence Summary: All-optical electrophysiology revealed the function in awake mice of an inhibitory microcircuit in barrel cortex Layer 1.

Main Text

The brain receives myriad sensory inputs from which it must distinguish the relevant from the irrelevant. An input can merit attention either through its intrinsic properties (novelty, salience) or through learned associations. The sparse interneurons of neocortical Layer 1 (L1) have been hypothesized as a hub for integrating these factors and modulating the underlying cortex (*1–3*). L1 interneurons receive direct thalamic (*2*, *4*, *5*), cortico-cortical (*6*, *7*), and neuromodulatory (cholinergic (*2*, *3*, *8*) and serotonergic (*8*, *9*)) inputs, the last mediated by fast ionotropic receptors. Activation of L1 interneurons exerts powerful control of underlying cortex by inhibiting deeper-lying interneurons, dis-inhibiting pyramidal neurons (*1–3*, *6*), and directly inhibiting pyramidal neurons dendrites (*2*, *10*, *11*). Despite the suggestive anatomy and influence on underlying cortex, little is known about information processing within L1, especially in awake animals.

bioRxiv preprint doi: https://doi.org/10.1101/614172; this version posted April 23, 2019. The copyright holder for this preprint (which was not certified by peer review) is the author/funder, who has granted bioRxiv a license to display the preprint in perpetuity. It is made available under aCC-BY-NC-ND 4.0 International license.

A core principle of neuronal network dynamics is maintenance of balance between excitation (E) and inhibition (I). For instance, during sensory processing in cortical layer 4 (L4) excitation driven by thalamic inputs is countered by feed-forward inhibition from parvalbumin (PV) interneurons (*12*, *13*). L1 interneurons receive inhibitory inputs both from other L1 interneurons (*5*, *14*, *15*) and from deeper Martinotti cells (*11*). It is not known how these inputs influence L1 activity *in vivo*.

Electrophysiological studies in L1 *in vivo* have been challenging due to the sparseness of neuronal cell bodies. While a few whole-cell patch clamp recordings have been performed in anesthetized rats (*1*, *4*), technical difficulties have prevented similar acquisitions in awake animals. Due to their multimodal temporally precise inputs (*16*) and temporally precise outputs, one would like to measure the sub-threshold dynamics and spike timing of L1 neurons with high precision. Recent advances in genetically encoded voltage indicators (GEVIs) enabled voltage imaging with single-neuron, single-spike resolution in hippocampus (*17–20*) and in superficial cortex (*18*, *19*) *in vivo*, opening the possibility for optical explorations of L1 circuit function *in vivo*.

Voltage alone does not distinguish the relative contributions of E and I synaptic inputs, yet this distinction is critical for understanding circuit mechanisms. A commonly used patch clamp technique is to inject current to achieve different levels of baseline depolarization and thereby to shift the relative driving force of E vs. I post-synaptic currents, revealing their distinct contributions (*21*). We previously paired near infrared GEVIs based on Archaerhodopsin 3 (Arch) with channelrhodopsin stimulation for optical measurements of excitability *in vivo* (Optopatch) (*17*, *22*) and of synaptic transmission in primary culture and acute slices (*23*). Here we show that optogenetic depolarization of a postsynaptic neuron during sensory processing *in vivo* can unmask otherwise hidden inhibitory inputs. We combine a novel holographic structured illumination imaging system, an Archaerhodospsin-derived GEVI optimized for crosstalk-free *in vivo* Optopatch, and patterned optogenetic stimulation to study the role of excitatory, inhibitory and neuromodulatory inputs on the function of the cortical L1 microcircuit during sensory processing in awake mice.

Results

In vivo Optopatch with holographic patterned illumination

Archon1 is an Arch-derived GEVI with improved trafficking and brightness (*24*). A soma-localized variant, SomArchon, enabled voltage imaging *in vivo* with good signal-to-noise ratio (*20*). We made a Cre-dependent bicistronic construct for co-expression of SomArchon and a blue light-activated soma-localized channelrhodopsin, CheRiff (*25*). We call this combined construct Optopatch4.

Voltage signals in tissue arise solely from the neuronal membrane. Illumination that enters the tissue but misses the membrane of interest contributes to background fluorescence and heating, but not to signal. In epifluorescence images of membrane-labeled neurons, the soma perimeter appears brighter than the center, a geometrical projection effect from viewing membranes edge-on. We thus reasoned that incident photons would most efficiently produce signal if targeted to the soma perimeter. Confocal-like excitation combined with spatially filtered emission would also minimize optical crosstalk from out-of-focus cells. We built a holographic structured illumination system (*26*) to achieve this precisely targeted illumination with red (λ = 635 nm) light for excitation of SomArchon (Fig. 1A, Fig. S1, Table S1, Methods).

bioRxiv preprint doi: https://doi.org/10.1101/614172; this version posted April 23, 2019. The copyright holder for this preprint (which was not certified by peer review) is the author/funder, who has granted bioRxiv a license to display the preprint in perpetuity. It is made available under aCC-BY-NC-ND 4.0 International license.

SomArchon fluorescence from all holographically targeted spots was recorded simultaneously on a scientific CMOS camera. Spatial filters were applied digitally in post-processing to separate signal from background (Methods). A digital micromirror device (DMD) patterned blue illumination for targeted optogenetic stimulation (Fig. 1A, Fig. S1, Table S1).

We characterized the performance of the system by imaging SomArchon-expressing neurons *in vivo* in the cortex. Under wide-field red illumination, the cells were not visible due to high background from scattered light (Fig. 1B). Targeted illumination revealed individual cells (Fig. 1B, Fig. S2). Holographic membrane-targeted illumination provided substantially better optical sectioning and signal-to-background ratio than did soma-wide illumination (Fig. S2). The combination of SomArchon and the holographic optical system enabled recording of spontaneous action potentials with SNR 12 ± 4 (mean ± s.d., n = 16 cells) at depths between 20 and 150 μm and SNR 6.7 at a depth of ~200 μm in awake head-fixed mice (Fig. S3, Methods).

To target expression to L1, we expressed Optopatch4 in 5HT$_{3A}$R-Cre mice (Fig. 1C, D). This line drives expression predominantly in supragranular layers, including in ~90% of L1 interneurons (*2*, *9*). Recordings targeting L1 neurons were performed at a depth < 150 μm. Two-photon fluorescence images of an appended eGFP tag showed membrane-localized and somatically restricted expression in L1 (Fig. 1E). In acute slices, targeted optogenetic stimuli evoked characteristic firing patterns in L1 neurons, including previously reported bursting adapting and late-spiking non-adapting phenotypes (*14*) (Fig. S4).

In head-fixed mice, targeted optogenetic stimuli evoked spikes which were clearly resolved via holographically targeted voltage imaging in recordings acquired at a 1 kHz frame-rate (Fig. 1F). We measured excitability and firing properties of L1 neurons in mice anesthetized with isoflurane, and then later re-measured the same neurons in awake mice (Fig. S5). While awake mice tended to show higher excitability and more variable subthreshold dynamics, the core firing properties (e.g. bursting, adaptation) were preserved within each cell between the two brain states (Fig. S5).

Voltage imaging of whisker stimulus-triggered activity in L1 neurons

Barrel fields corresponding to individual whiskers (B2, C2, D2) were identified by intrinsic imaging (Fig. S6, Methods). We then used voltage imaging to characterize the sensory-evoked responses in L1 interneurons. In both anesthetized and awake mice, brief stimuli to individual whiskers (~1 mm deflection, ~8 mm from the base, 20 ms duration, repeated at 0.5 Hz, Methods) elicited excitatory post-synaptic potentials (EPSPs) and often spikes in L1 neurons in the corresponding barrel fields (Fig. 1G, H). The delay from stimulus onset to spike peak was 16 ± 2 ms (mean ± s.d., n = 135 events, 24 neurons, 3 mice) in anesthetized mice and 16 ± 3 ms in awake mice (mean ± s.d., n = 73 events, 21 neurons, 3 mice, Fig. 1J, K). Similar delay and jitter were previously reported in L4 pyramidal neurons and fast-spiking neurons, both of which receive direct thalamic inputs (*12*).

In a comparison between spontaneous and whisker-evoked spikes, we observed striking differences in the mean subthreshold dynamics calculated via a spike-triggered average (STA, Fig. 1I, L). Spontaneous spikes rode atop a baseline depolarization that both preceded and followed the spike, whereas whisker-evoked spikes arose abruptly and were followed by a period of hyperpolarization (Fig. 1I, L). Stimulus-triggered average waveforms of trials that did not induce spikes also showed a depolarization followed by a hyperpolarization (Fig. S7). Together,

bioRxiv preprint doi: https://doi.org/10.1101/614172; this version posted April 23, 2019. The copyright holder for this preprint (which was not certified by peer review) is the author/funder, who has granted bioRxiv a license to display the preprint in perpetuity. It is made available under aCC-BY-NC-ND 4.0 International license.

these results suggested that the hyperpolarization was due to a sensory stimulus-evoked network-level inhibition, and not due to a spike-driven cell-autonomous afterhyperpolarization.

STA waveforms also differed between anesthetized and awake animals (Fig. 1I, L). For spontaneous spikes, the subthreshold depolarization was larger under anesthesia than wakefulness (anesthetized: 22 ± 2% of spike height, n = 17 neurons, 3 mice vs. awake: 10 ± 2% of spike height, n = 22 neurons, 3 mice, $p = 3 \times 10^{-4}$, two-tailed t-test, mean ± s.e.m.). For whisker-evoked spikes, the after-spike hyperpolarization was smaller but longer lasting under anesthesia than under wakefulness than (anesthetized: 11 ± 2% spike height, n = 24 neurons, 3 mice vs. awake: 17 ± 1% of spike height, n = 21 neurons, 3 mice, p = 0.02, two-tailed t-test; anesthetized: 254 ± 15 ms recovery time vs. awake: 127 ± 14 ms, $p = 1 \times 10^{-7}$, two-tailed t-test, all mean ± s.e.m). These observations are consistent with a more depolarized resting potential under wakefulness (*27*).

Optical dissection of excitation and inhibition during sensory processing

Rapid inhibition is mediated by $GABA_A$ receptors, ligand-gated chloride channels with a reversal potential of ~-70 mV. L1 interneurons in anesthetized rats have been reported to rest at -65 to -70 mV (*4*), suggesting that inhibitory inputs should have only small effects on membrane potential at rest. Borrowing from well-established patch clamp protocols (*21*), we reasoned that optogenetic depolarization would increase the driving force for inward chloride current, and thereby amplify the impact of $GABA_A$ receptor activation on the inhibitory postsynaptic potential (IPSP) (Fig. 2A,B).

In both awake and anesthetized mice, whisker stimuli in the absence of optogenetic stimulation evoked clear spikes or EPSPs in L1 interneurons, as in prior experiments (Fig. 2C, S8). Optogenetic stimuli targeted to the same cells one at a time (500 ms duration, 1.8 to 21 mW/mm^2, repeated at 1 Hz) reliably evoked stimulus intensity-dependent spiking. Remarkably, whisker stimuli applied during targeted single-cell optogenetic stimulation led to suppressed spiking, and hyperpolarization (Fig. 2C, D, E, S8). We quantified the sensory-evoked subthreshold waveforms by digitally removing spikes (Methods) and calculating a stimulus-triggered average at different optogenetic stimulus strengths (Fig. 2E, S8). In both awake and anesthetized brain states, whisker stimuli had opposite effects in the absence vs. presence of baseline optogenetic stimulation, illustrating dramatic non-additivity of sensory and optogenetic inputs to the same neuron.

A simple biophysical model containing passive leak, channelrhodopsin, AMPA receptor and $GABA_A$ receptor conductances captured the main features of our data (Fig. 2F, G, Methods). We assumed a transient excitatory synaptic input followed shortly by a transient inhibitory input. The model confirmed that optogenetic depolarization increased the driving force for chloride, revealing the presence of otherwise hidden sensory-evoked inhibitory inputs. Depolarization via endogenous currents, as occurred in the transition from anesthesia to wakefulness, also amplified the impact of transient inhibition, explaining the difference in whisker-evoked subthreshold waveforms in Figs. 1I, L.

Despite lacking many details (e.g. active conductances), the biophysical model captured several subtle aspects of the subthreshold dynamics. In the anesthetized state, the IPSP amplitude was significantly smaller under strong optogenetic drive than under weak drive (16 ± 4% of spike height at high optogenetic drive (21 mW/cm^2) vs. 29 ± 5% of spike height at low

bioRxiv preprint doi: https://doi.org/10.1101/614172; this version posted April 23, 2019. The copyright holder for this preprint (which was not certified by peer review) is the author/funder, who has granted bioRxiv a license to display the preprint in perpetuity. It is made available under aCC-BY-NC-ND 4.0 International license.

optogenetic drive (5.8 mW/cm^2), n = 15 neurons, 3 mice, p = 0.001, two-sided paired-sample t-test, mean ± s.e.m.). There was also a small, but not statistically significant, similar trend in the awake state (23 ± 4% of spike height at high optogenetic drive vs. 28 ± 4% of spike height at low optogenetic drive, n = 27 neurons, 4 mice, p = 0.19, two-sided paired-sample t-test). The model revealed that these decreases were due to shunting of the membrane potential toward CheRiff reversal potential (~0 mV), and attributed the difference between anesthesia and wakefulness to a lower membrane resistance under wakefulness (e.g. due to tonic synaptic inputs). The IPSP duration also became shorter under strong optogenetic drive in both awake and anesthetized brain states. The model ascribed this effect to a decreased membrane RC time-constant due to the high CheRiff conductance. Our simple model thus connected the complex context-dependent whisker-evoked responses in L1 neurons to basic membrane biophysical properties.

Temporal dissection of excitation and inhibition

We next asked about the relative timing of excitatory and inhibitory inputs. We delivered whisker stimuli alternately with and without baseline weak optogenetic stimulation targeted to single neurons (5.8 mW/mm^2, Fig. 2H). We anticipated that the whisker-evoked responses in these two conditions would initially coincide and then would diverge upon arrival of the inhibitory inputs. We compared stimulus-triggered average waveforms of trials that evoked spikes (Fig. 2I). The shape of the waveforms overlapped for the first 2 ms after onset of whisker-evoked depolarization. Thereafter, the waveform in the presence of optogenetic stimulation fell below the waveform in the absence, signaling the onset of inhibition (Fig. 2I, inset). This finding implies a ~2 ms delay between onset of excitation and inhibition, suggesting at most a difference of one synapse in the respective paths (*12*). This result does not rule out the possibility that slower inhibitory signals (e.g. from $GABA_B$ receptors or polysynaptic mechanisms) also contributed to inhibition at later times.

Lateral inhibition

We then sought to identify the source of the inhibition. Patch clamp measurements in acute slices have identified inhibitory connections between L1 interneurons (*5*, *14*, *15*). Since our whisker stimuli evoked spikes in arbitrarily selected cells with high probability and inhibition lagged excitation by only ~2 ms, we hypothesized that the rapid whisker stimulus-evoked inhibition was due to lateral connections within the L1 population.

To test this hypothesis, we performed an all-optical circuit-mapping experiment *in vivo* using patterned optogenetic stimulation (Fig. 3A). We expressed Optopatch4 in 5-HT_{3A}R-Cre mice and targeted voltage imaging to 1-3 L1 interneurons in the center of the field of view. We then defined two optogenetic stimulus patterns. The first pattern comprised small disks targeted individually to the central neurons. These disks were stimulated with long pulses of blue light (500 ms, 25 mW/mm^2), with the goal to depolarize the targeted cells and to increase the driving force for inhibitory currents. The second pattern comprised an annulus (inner diameter ~200 μm, outer diameter of ~400 μm, Fig. 3B, C, Methods), surrounding the central neurons. Midway through the stimulation of the central neurons, a brief flash (20 ms, 25 mW/mm^2) was applied to the neurons in the surrounding annulus to evoke synchronized spiking of the surrounding cells.

Optogenetic stimulation of the central neurons evoked robust spiking (spike rate 41 ± 6 Hz, n = 25 neurons, 3 mice, mean ± s.e.m.). Stimulation of the surrounding neurons transiently suppressed this spiking (spike rate 12 ± 4 Hz in the 25 ms following the annular flash, p = 4 ×

bioRxiv preprint doi: https://doi.org/10.1101/614172; this version posted April 23, 2019. The copyright holder for this preprint (which was not certified by peer review) is the author/funder, who has granted bioRxiv a license to display the preprint in perpetuity. It is made available under aCC-BY-NC-ND 4.0 International license.

10^{-4}, two-sided paired-sample *t*-test, Fig. 3D, E, F). The mean fluorescence waveform following the annular flash showed robust hyperpolarization of the central neurons (27 ± 3% of spike height, Fig. 3G, S9). (Control experiments without the central optogenetic stimulus revealed that the initial depolarization after the annular flash was an artifact from light scatter, Fig. S9). The spike patterns and subthreshold hyperpolarization dynamics in these experiments closely resembled the corresponding data for a sensory stimulus (Fig. 2E, F, I). These results are consistent with the model that sensory stimulation elicits rapid activation of L1 neurons followed by rapid lateral inhibition.

Neuromodulation

Finally, we explored the role of neuromodulatory activity on L1 dynamics (Fig. 4A). A mild air puff to the face has been shown to activate cholinergic neurons in basal forebrain (*16*), and these neurons are known to innervate cortical L1 (*3*, *28*). We imaged L1 neurons in awake mice while delivering a mild air puff (100 ms duration, ~5 psi) to the ipsilateral eye (to avoid incidental stimulation of whiskers associated with the imaged neurons, Fig. 4B). In 15 of 21 neurons, the air puff evoked a clear depolarization. In 6 of these neurons the air puff evoked one or more spikes and in 3 of these neurons, the air puff evoked a barrage of firing that lasted ~1 s, strikingly different from the precisely timed single spikes evoked by whisker stimulation (Fig. 4C). To resolve the subthreshold dynamics, we digitally removed spikes and calculated the air puff-triggered average across all imaged neurons. The air puff evoked a depolarization that grew over ~100 ms, reached 20 ± 3% of spike height, and decayed with a ~1600 ms recovery time (Fig. 4E). When the air puff was paired with optogenetic stimulation (500 ms, 5.8 mW/mm^2), we did not observe a significant change in population-average spike rate associated with the air puff (Fig. 4D). Some neurons increased their spike rate while others appeared to enter depolarization block (see e.g. Fig. 4C, second and fourth traces), both effects attributable to increased excitation. The subthreshold voltage showed a depolarizing transient (Fig. 4E), opposite to the response to a whisker stimulus (e.g. Fig. 2C).

Together, these results implied that the air puff evoked a predominantly excitatory subthreshold input without paired inhibition. Considering the heterogeneous neural responses to the air puff, it is possible that the air puff primarily activated a subset of L1 neurons that did not have strong inhibitory connections within L1; alternatively, the predominantly subthreshold and asynchronous responses may not have driven enough synchronous spiking to elicit detectable inhibition in L1.

The α4 nicotinic acetylcholine receptor is highly expressed in L1 interneurons (*2*, *29*). We made paired recordings of the same L1 interneurons before and after systemic administration of the α4 nAChR blocker dihydro-β-erythroidine hydrobromide (DHβE, 1.5 mg/kg i.p., Fig. 4F). This drug did not significantly affect the spike rate (Fig. 4G), but it largely suppressed the air puff-induced depolarization, consistent with a cholinergic mechanism for this effect (amplitude, A. U., 0.22 ± 0.04 before vs 0.10 ± 0.03 after drug, n = 15 neurons, 3 mice, p = 0.02, two-sided paired-sample *t*-test, Fig. 4H, I).

Discussion

All-optical electrophysiology can report both the nature of the synaptic inputs (E vs. I) and the spiking output of a cell, revealing the transformation that the cell implements. Optogenetic

bioRxiv preprint doi: https://doi.org/10.1101/614172; this version posted April 23, 2019. The copyright holder for this preprint (which was not certified by peer review) is the author/funder, who has granted bioRxiv a license to display the preprint in perpetuity. It is made available under aCC-BY-NC-ND 4.0 International license.

stimulation and voltage imaging in distinct neural populations can reveal cell type-specific connections and their role in circuit dynamics. While we focused on rapid sensory processing, these tools may also prove useful in studies of neural plasticity, development and disease mechanisms.

Our experiments revealed that lateral inhibition among L1 interneurons mediates precisely timed single-spike responses to abrupt sensory inputs. A striking aspect of these findings was that the same sensory input (a whisker deflection) could elicit spikes in a hyperpolarized neuron, but decrease the mean spike rate in a depolarized neuron. This observation highlights the importance of considering electrophysiological context when interpreting functional data recorded *in vivo*. While our experiments used a channelrhodopsin to drive depolarization, ionotropic AMPA receptors (*30*), acetylcholine receptors (*31*), serotonin receptors (*32*) and channelrhodopsins (*33*) all have similar current-voltage relations, implying that baseline activation of any of these receptors could switch the sensory-evoked response of an L1 neuron from excitation-dominated to inhibition-dominated. Our results showed that thalamic and neuromodulatory excitation converge in L1 neurons, albeit with different temporal profiles. Whereas thalamic excitation led to synchronous spiking followed by network inhibition, neuromodulatory excitation evoked mainly subthreshold depolarizations or asynchronous spiking in a subset of cells, which did not induce network inhibition.

Together with prior anatomical and electrophysiological studies (*2*, *5*, *14*, *34*), our results suggest a simple picture for how L1 detects novel sensory stimuli (Fig. 5). While at least four genetically distinct sub-types of neurons exist in L1 (*11*, *15*), we consider here two broad classes based on firing properties and morphology. One population bursts readily, but quickly adapts (*14*, *15*). A second population is slow to spike, and does not adapt (*14*, *15*). Thalamic inputs drive both cell types. The late-spiking cells inhibit the bursting cells. The late-spiking neurons are primarily neurogliaform (eNGC) cells which synapse within L1, while the bursting cells are primarily VIP^+ single bouquet-like (SBC-like) cells which project to deeper areas, where they dis-inhibit underlying cortex. Thus a transient input activates the output cells, while a tonic input predominantly drives lateral inhibition. Within this picture, the distinct intrinsic firing properties of the different L1 sub-types play a crucial role.

Experiments *in vivo* (*3*) and in slices (*35*) have shown that cholinergic stimulation elicits complex effects on L1 interneurons, but how these effects modulate sensory-evoked responses *in vivo* remains to be determined. A clear goal for future work will be to characterize the role that each subclass of L1 interneurons plays in sensory processing and integration of top-down information including cortico-cortical and neuromodulatory inputs.

Acknowledgments: We thank B. Sabatini for advice and discussion; G. Vargish and T. Hensch for the $5HT_{3A}R$-Cre mouse line; S. Begum, K. Williams, A. Preecha and H. Dahche for technical assistance; M. Gomez-Ramirez and C. Moore for advice on whisker stimulation; H. Pi for advice on air puff; B. Gmeiner for advice on optics; Y. Adam for advice on mouse surgeries. **Funding:** This work was supported by the Howard Hughes Medical Institute. **Author contributions:** L.Z.F., A.E.T. and A.E.C. conceived and designed the study. L.Z.F. designed and conducted the experiments, built the optical system, programed the software, analyzed the data and co-wrote the manuscript. S.K. and H.W. built the optical system in early stage. U.B. performed numerical simulations and data fitting. K.D.P. and E.S.B. shared SomArchon. V.P. helped with slice

bioRxiv preprint doi: https://doi.org/10.1101/614172; this version posted April 23, 2019. The copyright holder for this preprint (which was not certified by peer review) is the author/funder, who has granted bioRxiv a license to display the preprint in perpetuity. It is made available under aCC-BY-NC-ND 4.0 International license.

experiments. M.E.X. helped analyze the data. A.E.C. co-wrote the manuscript and supervised the research. **Competing interests:** A.E.C. is a founder of Q-State Biosciences.

Data and materials availability: Plasmids are available on Addgene. Data, code, and materials used in the analysis are available upon reasonable request to A.E.C..

Supplementary Materials:

Materials and Methods
Supplementary Text
Figs. S1 to S9
Table S1

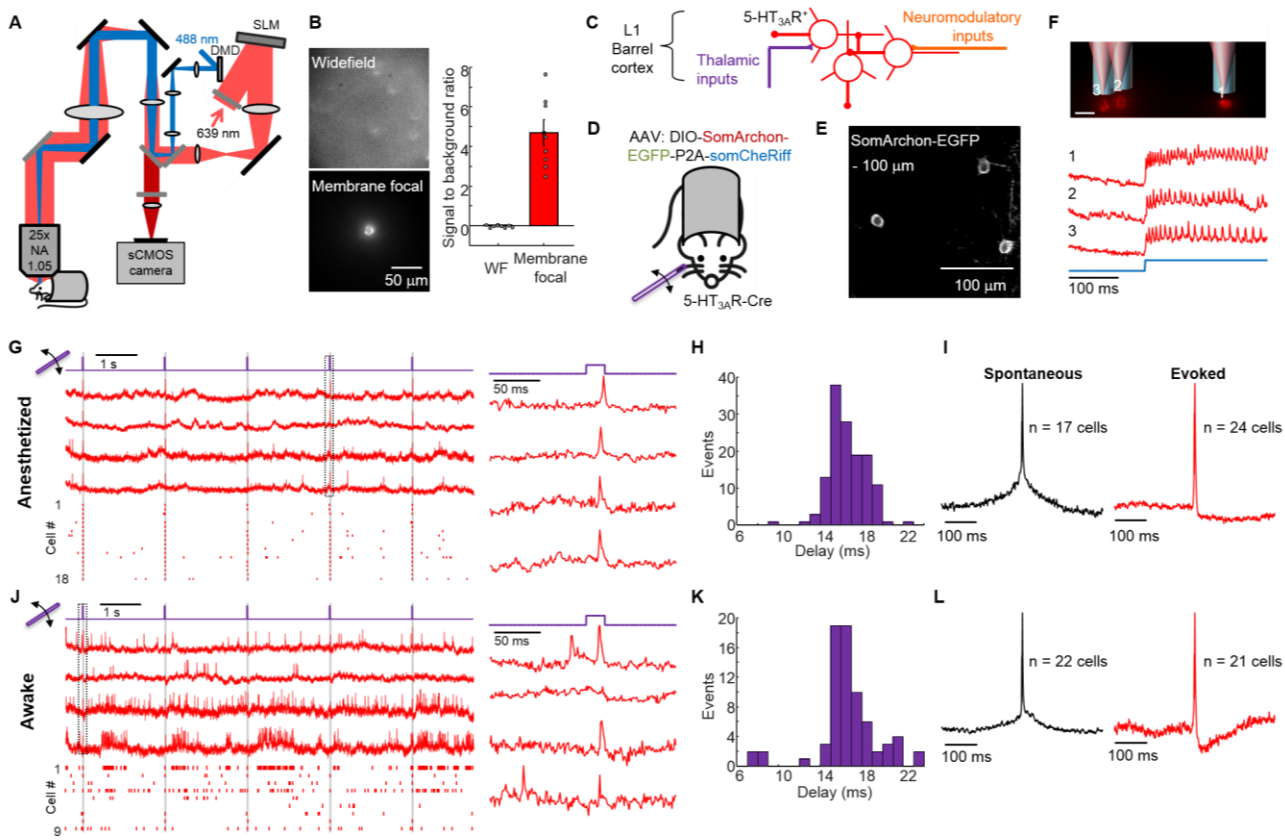

Figure 1. All-optical electrophysiology in L1 neurons *in vivo*. (**A**) Optical system for holographic structured illumination voltage imaging (red light) and micromirror-patterned optogenetic stimulation (blue light). Details in **Methods**. (**B**) Comparison of widefield epifluorescence and membrane-targeted holographic illumination of the same field of view containing a SomArchon-expressing L1 neuron. Scale bar 50 µm. Right: quantification of the signal-to-background ratio for the two imaging modalities. (**C**) 5-HT3AR-positive interneurons in L1 of the barrel cortex receive sensory inputs from the thalamus, neuromodulatory inputs from higher brain regions, and lateral inhibition from other L1 interneurons. (**D**) Virus encoding a cre-dependent construct for co-expression of a voltage indicator (SomArchon-EGFP) and an optogenetic actuator (somCheRiff) were injected into barrel cortex of 5-HT3AR-Cre mice. A

bioRxiv preprint doi: https://doi.org/10.1101/614172; this version posted April 23, 2019. The copyright holder for this preprint (which was not certified by peer review) is the author/funder, who has granted bioRxiv a license to display the preprint in perpetuity. It is made available under aCC-BY-NC-ND 4.0 International license.

glass capillary delivered small stimuli to an individual whisker. (**E**) Two-photon microscopy image of GFP fluorescence from SomArchon-EGFP in barrel cortex L1 showing good trafficking and soma localization. Scale bar: 100 µm, image depth 100 µm below dura. (**F**) Combination of patterned optogenetic stimulation (blue) and holographic illumination for voltage imaging. Scale bar 10 µm. Bottom: fluorescence traces from the three indicated cells in response to a step in blue illumination in an anesthetized mouse. (**G**) Fluorescence transients in single L1 interneurons evoked by whisker stimuli (20 ms deflections at 0.5 Hz) in anesthetized mice. Left, top: examples fluorescence traces recorded at 1 kHz frame rate. Traces have been corrected for photobleaching but not otherwise filtered. Bottom: raster plot showing spikes from n = 18 neurons Right: Fluorescence waveforms from the boxed region at left. (**H**) Distribution of delays between stimulus onset and peak of evoked spike. (**I**) Spike-triggered average waveform of spontaneous (left) and whisker stimulus-evoked (right) action potentials. A spike was classified as 'evoked' if it occurred within 30 ms of stimulus onset. (**J-L**) Same as **G-I** but in an awake mouse. Data in **G-L** recorded from 3 mice.

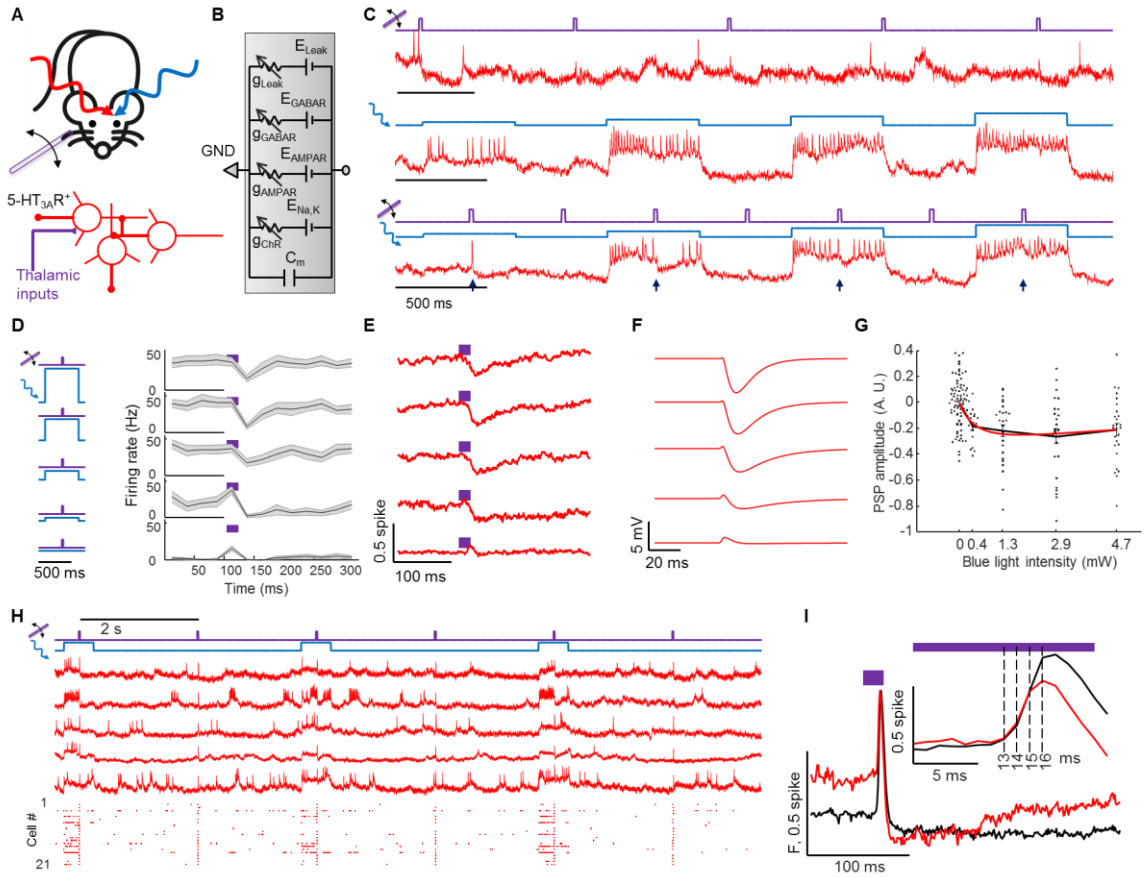

Figure 2. **Optical dissection of excitation and inhibition in L1 interneurons in awake mice.** (**A**) Whisker stimuli and single cell-targeted optogenetic stimuli were paired in 5HT$_{3A}$R-Cre mice expressing Optopatch4. (**B**) Conductance-based model of membrane potential. This simple model only contains passive conductances, with gating by light (Channelrhodopsin, ChR), glutamate (AMPAR), and GABA (GABAR). A leak conductance sets the resting potential of the cell in the absence of optogenetic or synaptic inputs. (**C**) Three recordings from

bioRxiv preprint doi: https://doi.org/10.1101/614172; this version posted April 23, 2019. The copyright holder for this preprint (which was not certified by peer review) is the author/funder, who has granted bioRxiv a license to display the preprint in perpetuity. It is made available under aCC-BY-NC-ND 4.0 International license.

a single neuron showing response to (top) whisker stimulus, (middle) optogenetic stimulus, and (bottom) simultaneous optogenetic and whisker stimuli. Arrows show whisker stimulus-evoked inhibition. (**D**) Mean spike rate evoked by whisker stimuli atop different levels of optogenetic stimulus. In the absence of optogenetic stimulation, whisker stimuli evoked precisely timed single spikes. In the presence of optogenetic stimulation, whisker stimuli suppressed spiking. The suppression decreased in amplitude and duration as the strength of the optogenetic stimulus increased. Shading represents s.e.m. from n = 27 neurons, 4 mice. (**E**) Mean whisker stimulus-evoked subthreshold waveforms at different levels of optogenetic drive. Spikes were digitally removed prior to averaging (Methods). (**F**) Simulated membrane voltage waveforms under different levels of optogenetic drive, using the model shown in (B). Excitation was assumed to lead inhibition by 2 ms. Details in Methods. (**G**) Comparison of PSP amplitude as a function of optogenetic stimulus strength with numerical simulation from a simple conductance-based model. (**H**) Repetitive measurements of whisker stimulus-evoked responses in anesthetized mice, with and without baseline optogenetic stimulation. Top: example recordings. Bottom: spike raster from n = 21 neurons, 3 mice. (**I**) Mean fluorescence responses to whisker stimulus without (black) and with (red) baseline optogenetic stimulation. Traces have been aligned to their peak. Inset: delay between onset of excitation (between 13 and 14 ms) and onset of inhibition (between 15 and 16 ms). To facilitate comparison, traces were vertically offset to align baseline values.

bioRxiv preprint doi: https://doi.org/10.1101/614172; this version posted April 23, 2019. The copyright holder for this preprint (which was not certified by peer review) is the author/funder, who has granted bioRxiv a license to display the preprint in perpetuity. It is made available under aCC-BY-NC-ND 4.0 International license.

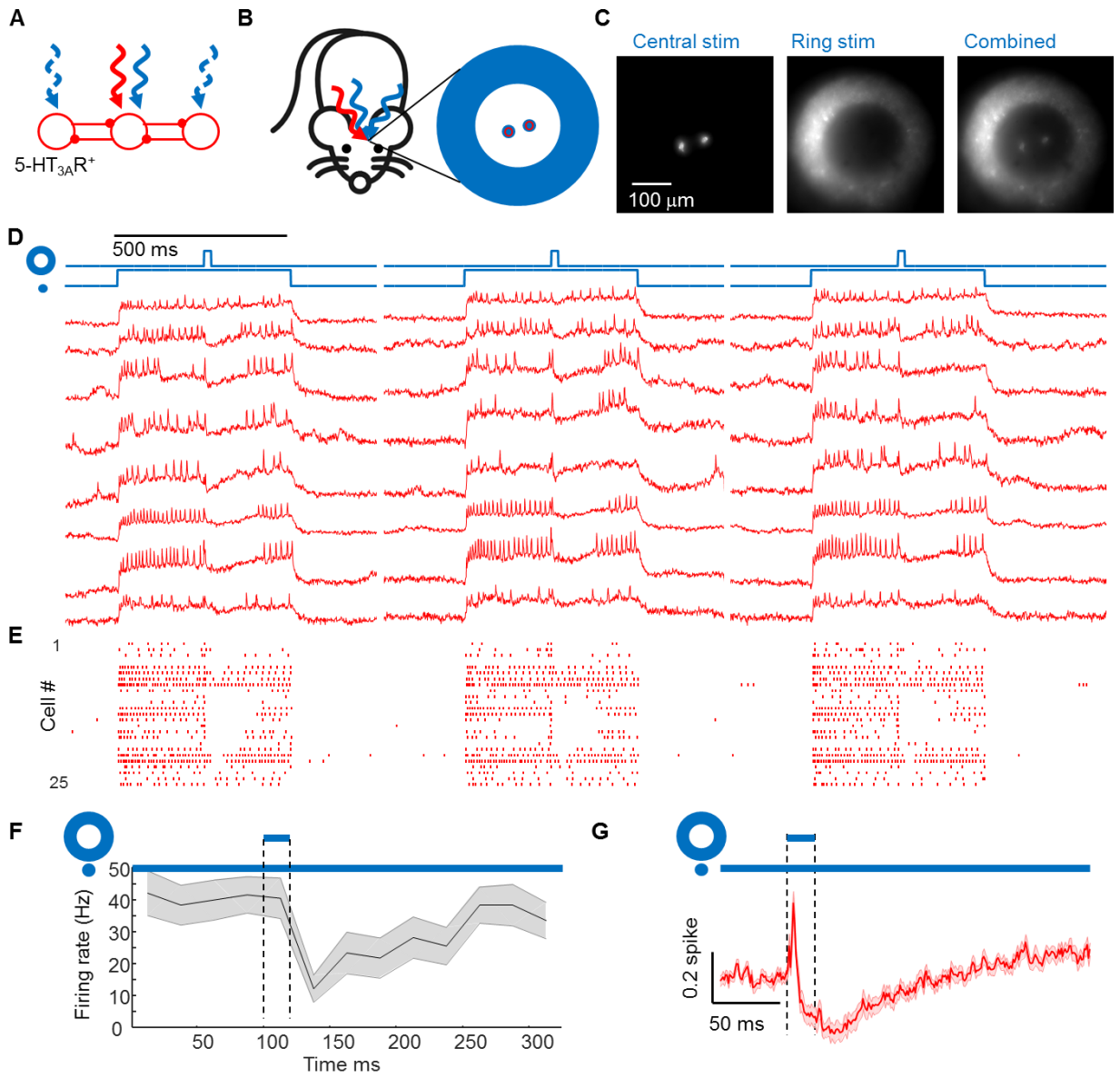

Figure 3. Center/surround optogenetic stimulation reveals lateral inhibition in L1. (**A**) Simple model of L1 circuit with lateral inhibition. Tonic optogenetic stimulation depolarizes the central neuron, increasing the driving force for inhibitory currents. Pulsed optogenetic stimulation of the surrounding neurons evokes lateral inhibition, revealed by voltage imaging (red) in the central neuron. (**B**) Experiment to probe lateral inhibition in L1. 5-HT$_{3A}$R-Cre mice expressed Optopatch4 in barrel cortex. Optogenetic stimuli were delivered separately to central and surrounding neurons. Voltage imaging was performed only in central neurons. Experiments were performed in anesthetized mice. (**C**) Epifluorescence images showing the illumination patterns *in vivo*. Scale bar 100 µm. (**D**) Fluorescence waveforms from the central neurons under center/surround optogenetic stimulation. Central stimulation depolarized the targeted neurons and evoked spiking. Surround stimulation hyperpolarized the targeted neurons and suppressed spiking. (**e**) Spike raster showing responses from n = 25 neurons, 3 mice. (**F**) Mean spike rate during central stimulation, before and after surround stimulation. Surround stimulation caused

bioRxiv preprint doi: https://doi.org/10.1101/614172; this version posted April 23, 2019. The copyright holder for this preprint (which was not certified by peer review) is the author/funder, who has granted bioRxiv a license to display the preprint in perpetuity. It is made available under aCC-BY-NC-ND 4.0 International license.

spike rate to drop from 40.5 ± 6.3 Hz to 12.3 ± 4.1 Hz, n = 25 neurons, 3 mice ($p = 4\times10^{-4}$, two-sided paired-sample t-test). Shading represents s.e.m. (**G**) Mean subthreshold voltage during central stimulation, before and after surround stimulation. Surround stimulation caused inhibition in the central neuron. The initial spike in membrane voltage in the central neuron was due to scattered light from the surround which drove direct CheRiff activation. Shading represents s.e.m..

bioRxiv preprint doi: https://doi.org/10.1101/614172; this version posted April 23, 2019. The copyright holder for this preprint (which was not certified by peer review) is the author/funder, who has granted bioRxiv a license to display the preprint in perpetuity. It is made available under aCC-BY-NC-ND 4.0 International license.

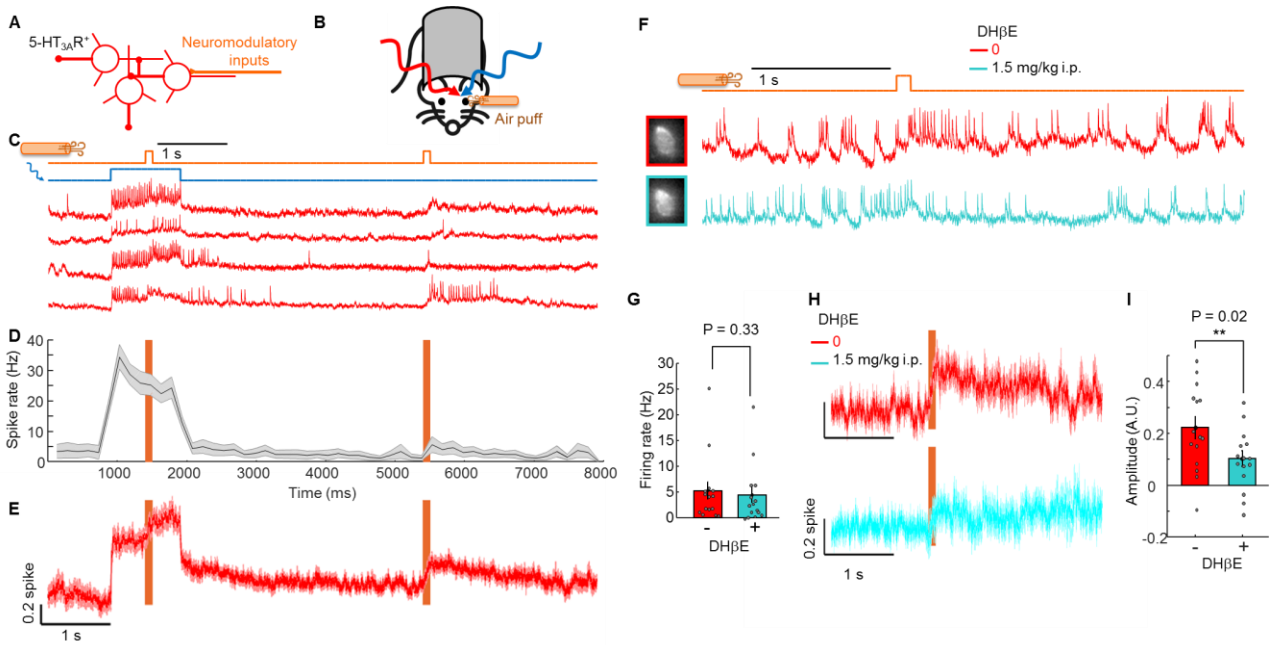

Figure 4. Cholinergic inputs drive excitation in L1 interneurons. (**A**) Schematic showing neuromodulatory inputs driving L1 interneurons. (**B**) Experiment to probe neuromodulatory effects in L1. Optopatch measurements were performed in barrel cortex L1 interneurons of awake 5-HT3AR-Cre mice while a mild air puff was applied to the ipsilateral eye. (**C**) Fluorescence recordings from single cells showing responses to air puff stimulation in the presence and absence of baseline optogenetic stimulation. (**D**) Mean spike rate during air puff stimulation with and without baseline optogenetic depolarization (n = 21 neurons, 4 mice). (**E**) Mean subthreshold response to air puff. Spikes were digitally removed from the traces. (**F**) Effect of a cholinergic blocker, DHβE, on the air puff response. Paired measurements were performed returning to the same cell before and after drug administration. (**G**) DHβE did not significantly affect spontaneous spike rate. (**H**) Mean subthreshold responses to air puff before and after administration of DHβE. (**I**) DHβE significantly reduced the subthreshold response to air puff, as quantified by the amplitude of the subthreshold response to air puff. Data in (G – I) from n = 16 neurons measured before and after drug administration, 3 mice.

bioRxiv preprint doi: https://doi.org/10.1101/614172; this version posted April 23, 2019. The copyright holder for this preprint (which was not certified by peer review) is the author/funder, who has granted bioRxiv a license to display the preprint in perpetuity. It is made available under aCC-BY-NC-ND 4.0 International license.

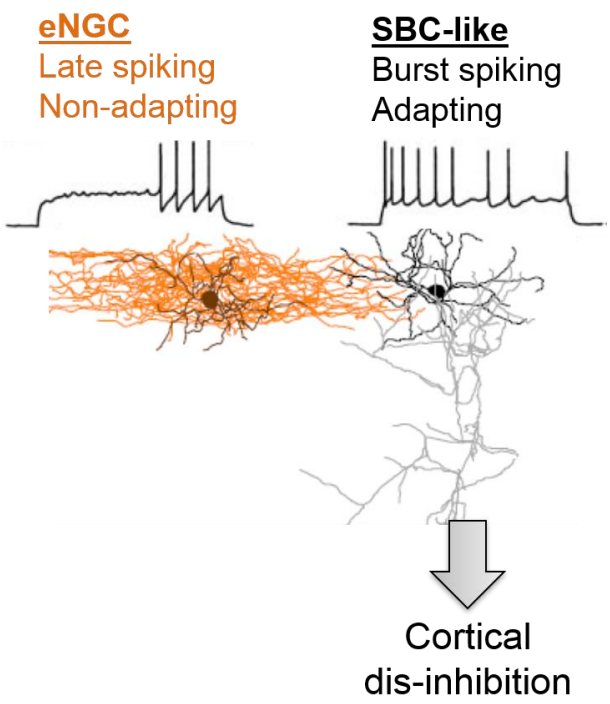

Figure 5. Simple model for novelty and salience detection in cortical L1. Downward-projecting SBC-like neurons dis-inhibit underlying cortex. These neurons are, in turn, inhibited by eNGC neurons. The distinct firing properties of these two sub-classes of neurons cause the circuit to function as a novelty detector. Image adapted from (Chu et al.J. *Neurosci* 23 (2003): 96-102.) and (Jiang et al. *Science* 350 (2015): aac9462).

bioRxiv preprint doi: https://doi.org/10.1101/614172; this version posted April 23, 2019. The copyright holder for this preprint (which was not certified by peer review) is the author/funder, who has granted bioRxiv a license to display the preprint in perpetuity. It is made available under aCC-BY-NC-ND 4.0 International license.

References:

1. X. Jiang, G. Wang, A. J. Lee, R. L. Stornetta, J. J. Zhu, The organization of two new cortical interneuronal circuits. *Nat. Neurosci.* **16**, 210–218 (2013).
2. A. E. Takesian, L. J. Bogart, J. W. Lichtman, T. K. Hensch, Inhibitory circuit gating of auditory critical-period plasticity. *Nat. Neurosci.* **21**, 218–227 (2018).
3. J. J. Letzkus *et al.*, A disinhibitory microcircuit for associative fear learning in the auditory cortex. *Nature*. **480**, 331–335 (2011).
4. Y. Zhu, Rapid Arrival and Integration of Ascending Sensory Information in Layer 1 Nonpyramidal Neurons and Tuft Dendrites of Layer 5 Pyramidal Neurons of the Neocortex. *J. Neurosci.* **24**, 1272–1279 (2004).
5. S. J. Cruikshank *et al.*, Thalamic control of layer 1 circuits in prefrontal cortex. *J. Neurosci.* **32**, 17813–17823 (2012).
6. S. Lee, I. Kruglikov, Z. J. Huang, G. Fishell, B. Rudy, A disinhibitory circuit mediates motor integration in the somatosensory cortex. *Nat. Neurosci.* **16**, 1662–1670 (2013).
7. L. M. Palmer *et al.*, The cellular basis of GABAB-mediated interhemispheric inhibition. *Science (80-.).* **335**, 989–993 (2012).
8. R. B. Poorthuis *et al.*, Rapid Neuromodulation of Layer 1 Interneurons in Human Neocortex. *Cell Rep.* **23**, 951–958 (2018).
9. S. Lee, J. Hjerling-Leffler, E. Zagha, G. Fishell, B. Rudy, The Largest Group of Superficial Neocortical GABAergic Interneurons Expresses Ionotropic Serotonin Receptors. *J. Neurosci.* **30**, 16796–16808 (2010).
10. A. J. Lee *et al.*, Canonical Organization of Layer 1 Neuron-Led Cortical Inhibitory and Disinhibitory Interneuronal Circuits. *Cereb. Cortex*. **25**, 2114–2126 (2015).
11. E. Abs *et al.*, Learning-Related Plasticity in Dendrite-Targeting Layer 1 Interneurons. *Neuron*. **100**, 684–699.e6 (2018).
12. L. Gabernet, S. P. Jadhav, D. E. Feldman, M. Carandini, M. Scanziani, Somatosensory integration controlled by dynamic thalamocortical feed-forward inhibition. *Neuron*. **48**, 315–327 (2005).
13. M. Wehr, A. M. Zador, Balanced inhibition underlies tuning and sharpens spike timing in auditory cortex. *Nature*. **426**, 442–446 (2003).
14. Z. Chu, M. Galarreta, S. Hestrin, Synaptic Interactions of Late-Spiking Neocortical Neurons in Layer 1. *J. Neurosci.* **23**, 96–102 (2003).
15. B. Schuman *et al.*, Four Unique Interneuron Populations Reside in Neocortical Layer 1. *J. Neurosci.* **39**, 125–139 (2018).
16. B. Hangya, S. P. Ranade, M. Lorenc, A. Kepecs, Central Cholinergic Neurons Are Rapidly Recruited by Reinforcement Feedback. *Cell*. **162**, 1155–1168 (2015).

bioRxiv preprint doi: https://doi.org/10.1101/614172; this version posted April 23, 2019. The copyright holder for this preprint (which was not certified by peer review) is the author/funder, who has granted bioRxiv a license to display the preprint in perpetuity. It is made available under aCC-BY-NC-ND 4.0 International license.

17. Y. Adam *et al.*, All-optical electrophysiology reveals brain-state dependent changes in hippocampal subthreshold dynamics and excitability. *bioRxiv*, 281618 (2018).

18. M. Chavarha *et al.*, Fast two-photon volumetric imaging of an improved voltage indicator reveals electrical activity in deeply located neurons in the awake brain. *bioRxiv*, 445064 (2018).

19. A. S. Abdelfattah *et al.*, Bright and photostable chemigenetic indicators for extended in vivo voltage imaging. *bioRxiv*, 436840 (2018).

20. Kiryl D. Piatkevich, Seth Bensussen, Hua-an Tseng, Sanaya N. Shroff, Violeta Gisselle Lopez-Huerta, Demian Park, Erica E. Jung, Or A. Shemesh, Christoph Straub, Howard J. Gritton, Michael F. Romano, Emma Costa, Bernardo L. Sabatini, Zhanyan Fu, Edward S. Boyden, Xue Han, Population imaging of neural activity in awake behaving mice.

21. M. Segal, J. L. Barker, Rat hippocampal neurons in culture: voltage-clamp analysis of inhibitory synaptic connections. *J. Neurophysiol.* **52**, 469–487 (1984).

22. S. Lou *et al.*, Genetically Targeted All-Optical Electrophysiology with a Transgenic Cre-Dependent Optopatch Mouse. *J. Neurosci.* **36**, 11059–11073 (2016).

23. L. Z. Fan *et al.*, All-optical synaptic electrophysiology probes mechanism of ketamine-induced disinhibition. *Nat. Methods*. **15**, 823–831 (2018).

24. K. D. Piatkevich *et al.*, Publisher Correction: A robotic multidimensional directed evolution approach applied to fluorescent voltage reporters. *Nat. Chem. Biol.* (2018), p. 1.

25. D. R. Hochbaum *et al.*, All-optical electrophysiology in mammalian neurons using engineered microbial rhodopsins. *Nat. Methods*, 1–34 (2014).

26. C. Lutz *et al.*, Holographic photolysis of caged neurotransmitters. *Nat. Methods*. **5**, 821–827 (2008).

27. C. M. Constantinople, R. M. Bruno, Effects and mechanisms of wakefulness on local cortical networks. *Neuron*. **69**, 1061–1068 (2011).

28. E. Eggermann, Y. Kremer, S. Crochet, C. C. H. Petersen, Cholinergic Signals in Mouse Barrel Cortex during Active Whisker Sensing. *Cell Rep.* **9**, 1654–1660 (2014).

29. S. Arroyo, D. Aziz, C. Bennett, S. Hestrin, S. P. Brown, Prolonged Disynaptic Inhibition in the Cortex Mediated by Slow, Non- 7 Nicotinic Excitation of a Specific Subset of Cortical Interneurons. *J. Neurosci.* **32**, 3859–3864 (2012).

30. N. Burnashev, H. Monyer, P. H. Seeburg, B. Sakmann, Divalent ion permeability of AMPA receptor channels is dominated by the edited form of a single subunit. *Neuron*. **8**, 189–198 (1992).

31. M. Ballivet *et al.*, Electrophysiology of a chick neuronal nicotinic acetylcholine receptor expressed in xenopus oocytes after cDNA injection. *Neuron*. **1**, 847–852 (1988).

32. N. K. McKinnon, D. C. Reeves, M. H. Akabas, 5-HT3 receptor ion size selectivity is a property of the transmembrane channel, not the cytoplasmic vestibule portals. *J. Gen. Physiol.* **138**, 453–466 (2011).

33. H. Zhang, E. Reichert, A. E. Cohen, Optical electrophysiology for probing function and pharmacology of voltage-gated ion channels. *Elife*. **5** (2016), doi:10.7554/elife.15202.

bioRxiv preprint doi: https://doi.org/10.1101/614172; this version posted April 23, 2019. The copyright holder for this preprint (which was not certified by peer review) is the author/funder, who has granted bioRxiv a license to display the preprint in perpetuity. It is made available under aCC-BY-NC-ND 4.0 International license.

34. Y. Zhu, Rapid Arrival and Integration of Ascending Sensory Information in Layer 1 Nonpyramidal Neurons and Tuft Dendrites of Layer 5 Pyramidal Neurons of the Neocortex. *J. Neurosci.* **24**, 1272–1279 (2004).

35. G. G. Turrigiano, K. R. Leslie, N. S. Desai, L. C. Rutherford, S. B. Nelson, Activity-dependent scaling of quantal amplitude in neocortical neurons. *Nature*. **391**, 892–896 (1998).